Unsupervised Spatial Embedded Deep Representation of Spatial Transcriptomics

Huazhu Fu[1, *], Hang Xu[2, *], Kelvin Chong[2], Mengwei Li[2], Kok Siong Ang[2], Hong Kai Lee[2], Jingjing Ling[2], Ao Chen[3], Ling Shao[1], Longqi Liu[3], Jinmiao Chen[2, †]

[1] Inception Institute of Artificial Intelligence, Abu Dhabi, United Arab Emirates

[2] Singapore Immunology Network (SIgN), Agency for Science, Technology and Research (A*STAR), 8A Biomedical Grove, Immunos Building, 138648, Singapore

[3] BGI-ShenZhen, Shenzhen 518103, China.

*These authors contributed equally to this work.

†Corresponding author. Email: chen_jinmiao@immunol.a-star.edu.sg

Key words: spatial transcriptomics; graph convolutional network; gene expression; deep learning

Abstract

In the past decade, single cell technologies have revolutionized our ability to study cellular heterogeneity. Spatial omics represents the next technological wave, granting spatial context to single cell transcriptomes. Integration analysis of transcripts and spatial information will greatly enable us to dissect tissue organization and inter-cellular communications. Here, we present SEDR, an unsupervised spatial embedded deep representation of both transcript and spatial information. The SEDR pipeline uses a deep autoencoder to construct a gene latent representation in a low-dimensional latent space, which is then simultaneously embedded with the corresponding spatial information through a variational graph autoencoder. SEDR was tested on the 10x Genomics Visium spatial transcriptomics and Stereo-seq datasets, demonstrating its ability to create a better data representation that benefits various follow-up analysis tasks. In benchmarking test, SEDR achieved better clustering accuracy than contemporary methods, and in conjunction with trajectory analysis, it correctly retraced retraces the prenatal development of the human dorsolateral prefrontal cortex. We also found the SEDR representation to be eminently feasible for batch integration. Finally, we used SEDR to characterize the intratumoral heterogeneity of human breast cancer. We identified regions with different immune microenvironments, ranging from pro-inflammatory to immune suppressive areas with infiltrated tumor associated macrophages (TAMs). Analysis suggested a cancer cell dissemination trajectory from cells in pre-metastatic state to invasive carcinoma.

Introduction

Single-cell omics technologies enable measurements at single cell resolution, leading to discoveries of new subpopulations across various tissues, in both healthy and diseased states. However, tissue dissociation into single cells prior to high throughput omics data acquisition leads to cellular spatial information being lost, hindering our dissection of spatial organization and intercellular interactions of individual cells. While computational tools have been developed to predict cell-cell interactions from ligand and receptor expression, they require validation using immunohistochemistry (IHC) or immunofluorescence (IF). Emerging spatial omics technologies overcome these limitations through simultaneous measurements of gene/protein expression and spatial location of cells. Such spatially-resolved transcriptomes of histological tissues enable the reconstruction of tissue architecture and cell-cell interactions[1,2,3,4,5,6,7,8,9] . This approach has proven its value in many applications including studies on brain disorders[2,10], tumour microenvironment[3,11], and embryonic development[12].

Among currently available spatial transcriptomics approaches, *in situ* capturing-based technologies such as 10x Genomics Visium and Nanostring GeoMX DSP have gained more popularity owning to their accessibility and ability to profile a large number of mRNA targets within each spot. In principle, a histological section from a tissue sample is permeabilized and the released mRNA is captured by either spatially-arrayed oligos on slide surfaces or by pre-hybridized RNA-target barcodes in manually defined regions of interest (ROI). However, both technologies suffer from limitations in the size of mRNA capture area, where the smallest size is typically ~50μm, which is larger than the diameter of a single cell. To overcome this limitation, computational methods have been developed to deconvolute the cell mixture of spatial spot[13,14,15,16,17,18,19,20]. Recently, improvements in mRNA capture methods have led to smaller subcellular capture areas that are ~1-10μm in diameter. These high-resolution spatial transcriptomics methods can obtain spatially-resolved transcriptomes with increased spatial fidelity but without any compromise in the number of genes captured. These methods include

Slide-seq[8], DBiT-seq[9], with the highest resolution (~1μm) thus far obtained by Stereo-seq[5], PIXEL-seq[6], and Seq-Scope[7]. These submicrometer-resolution methods usually require voxel binning or cell segmentation to produce a gene-by-cell expression matrix for downstream analysis. Recent technologies have also improved on the size of captured area and thus increased cell throughput, necessitating new computational methods that can handle big spatial data.

When analyzing spatial transcriptomics data, combining both gene expression and spatial information to learn a discriminative representation for each cell or spot is crucial. However, established workflows, e.g., Seurat[21], still employs pipelines for single-cell RNA-seq analysis, which primarily focus on gene expression data and ignore the spatial neighborhood structural relationship. Recently, several new methods have been developed for spatial transcriptomics to overcome this limitation. For example, BayesSpace[22] creates a model starts from a Markov Random Filed (MRF) priors which hypothesizes that spots belong to same cell type should be closer to one another and updates models with Bayesian approach. Giotto[23] implements a hidden Markov random filed (HMRF) model to detect domains with coherent patterns by comparing gene expression between cells and their neighbors. SpaGCN[24] uses graph convolutional network (GCN) to integrate gene expression, spatial location and histology in spatial transcriptomics data analysis. But the algorithm that SpaGCN integrates histology with spatial location is oversimplified and more evidence should be provided to support its rationality. stLearn[25] developes a Spatial Morphological gene Expression (SME) normalization method to normalize spatial omics data. Standard Louvain clustering algorithm is implemented to do unsupervised clustering on SME normalized data. Then stLearn divides broad clusters into sub-clusters according to spatial information if broad clusters spread into several locations. The strategy of stLearn may not make full usage of spatial omics data, because it integrates morphology and spatial information separately at normalization and clustering steps. In general, all stat-of-the-art methods have limitations for properly integration of spatial and morphological information. Moreover, the downstream analyses often require proper low-

dimension representation features of the data, which is either neglected or not optimized by state-of-the-art methods.

In this work, we developed an unsupervised spatial embedded deep representation (SEDR) method for learning a low-dimensional latent representation of gene expression embedded with spatial information. Our SEDR method consists of two main components, a deep autoencoder network for learning a gene representation, and a variational graph autoencoder network for embedding the spatial information. These two components are optimized jointly to generate a latent representation for spatial transcriptomics data analysis. We applied SEDR on the 10x Genomics Visium spatial transcriptomics dataset and demonstrated its ability to achieve better representation for various follow-up analysis tasks including clustering, visualization, trajectory inference and batch effects correction.

Results

Overview of SEDR.

SEDR learns a gene representation in a low-dimensional latent space with jointly embedded spatial information. As shown in Figure 1, given spatial transcriptomics data, SEDR first learns a nonlinear mapping from the gene expression space to a low-dimensional feature space using a deep autoencoder network. Simultaneously, a variational graph autoencoder is utilized to aggregate the gene representation with the corresponding spatial neighboring relationships to produce a spatial embedding. Then, the gene representation and spatial embedding are concatenated to form the final latent representation used to reconstruct the gene expression. Thereafter, an unsupervised deep clustering method[26] is employed to enhance the compactness of learned latent representation. This iterative deep clustering generates a soft clustering by assigning cluster-specific probabilities to each cell, leveraging the inferences between cluster-specific and cell-specific representation learning. Finally, the learned latent representation can be applied towards various analyzing tasks.

Quantitative assessment of SEDR on human dorsolateral prefrontal cortex (DLPFC) dataset.

To perform a quantitative comparison between SEDR and other methods, we downloaded the 10x Genomics Visium spatial transcriptomics data and the manually annotated layers for LIBD human dorsolateral prefrontal cortex (DLPFC) data[2]. The LIBD data includes 12 slices from the human DLPFC that spans six cortical layers plus white matter. We chose this dataset because the human DLPFC has clear and established morphological boundaries which can serve as the ground truth. We first applied the Seurat standard pipeline[21] to process and cluster cells using only expression profiles and set the result as the baseline result to benchmark SEDR, in order to investigate the extent to which spatial information improves cell clustering. Moreover, there are some methods that can integrate spatial information and RNA-seq data, including Giotto[23], stLearn[25], SpaGCN[24], and BayesSpace[22]. To compare SEDR with these methods, we also employed them to process the same dataset with the recommended default parameters.

In slice 151673 (Figure 2A) with 3,639 spots and 33,538 genes, SEDR and BayesSpace had the best performance in terms of both layer borders and ARI. When comparing the results on all 12 DLPFC samples, SEDR had the highest mean ARI (0.426) (Figure 2A bottom right), though the difference between SEDR and BayesSpace (0.418) was not significant (Mann-Whitney U Test[27]: p-value=0.78). Given the fact that BayesSpace is optimized for clustering, while the objective function of SEDR is to find the best latent representation, comparable clustering performance of SEDR and BayesSpace might indicate that SEDR makes better use of spatial information and gene expression. Besides clustering, BayesSpace does not produce latent representation, in contrast, SEDR derived embedding can be used for not only clustering but also various down-stream analysis tasks such as UMAP visualization, trajectory inference and batch effect correction, and thus provides more flexibility and utilities. Similar to SEDR, SpaGCN also uses GCN to process spatial transcriptomics data. Moreover, it incorporates histology information which is not included in SEDR. However, the clustering performance of

147 SEDR is better than SpaGCN (Mann-Whitney U Test p-value < 0.05). stLearn also integrates
148 histology data, but the performance is likewise poorer. This may indicate that the current
149 approaches utilized by SpaGCN and stLearn to incorporate histological data is not optimal. To
150 make full usage of histology information, we may need to treat it as a separate data modality
151 and use dedicated multi-view algorithms for integration.
152 SEDR generates a set of low dimensional representation features which can be used in
153 various down-stream analyses, such as trajectory inference[28]. Here, we used Monocle3[29] to
154 perform trajectory inference on sample 151673 with the Seurat output (RNA-only) and the
155 SEDR low dimensional representation features. We found that SEDR showed significantly
156 improved performance over Seurat (Figure 2B). In the UMAP plot of SEDR's output, cells
157 belonging to different layers were well-organized, and when we selected white matter (WM)
158 as the root, the pseudo-time reflected the correct "inside-out" developmental ordering of
159 cortical layers (Figure 2B). This demonstrated that compared to RNA-only analyses,
160 incorporating spatial information enabled SEDR to generate a better latent representation that
161 summarized the spatial transcriptomics data. We further confirmed our observations with
162 another trajectory inference method named PArtition-based Graph Abstraction (PAGA)[30]
163 using the SEDR-derived latent space embedding instead of UMAP coordinates (Figure 2C).
164 The PAGA results showed that the adjacent cortical layers tend to share greater similarity,
165 suggesting spatial adjacency is linked with transcriptomic and even functional similarity.
166 Notably, our trajectory is concordant with the chronological order of cortex development[31,32,33].
167 We then compared PAGA graphs generated using Seurat-derived principal components and
168 SEDR embedding. For each of 12 DLPFC slices, we calculated the ratio of weights of edges
169 between adjacent cortical layers over the total sum of weights of all edges. We found
170 significantly higher ratio by SEDR compared to Seurat (Mann-Whitney U test p-value < 0.05)
171 (Figure 2C right).

172 **SEDR corrects for batch effects.**

173 The proliferation of spatial omics application is generating ever increasing volumes of spatially

resolved omics data across different labs. However, differences in protocols and technologies complicate comparisons and data integration to produce consensus spatially resolved atlases of tissues. As with scRNA-Seq, removing batch effects in spatial omics dataset is a significant challenge. To date, there are no methods available for batch effects correction of spatial omics. Here, we demonstrate that SEDR is able to learn a joint embedding across multiple batches and project them into a shared latent space. Furthermore, it employs a DEC loss function that enables SEDR to retain biological variations while reducing technical variations. We evaluated the batch correcting performance of SEDR on the DLPFC datasets. We first assessed the batch variations among the 12 datasets and selected 3 sets (151507, 151672, 151673) which exhibit substantial batch effects. The common cortical layers from different batches were separated as shown in the UMAP plot (Figure 3A). We first applied Harmony to remove batch effects based on its superior performance in single-cell RNA-seq data integration[34]. Harmony was able to mix batches while keeping different layers apart; however, when zoomed into the individual layers, distinct batch-specific sub-clusters were still observable, suggesting that the batch effects were not completely removed (Figure 3B). Next, we applied SEDR on these 3 datasets and found that the batch effects were substantially reduced (Figure 3C). Common layers across batches were brought very close and were well-aligned, while different layers were minimally mixed. Further application of Harmony on the SEDR embedding evenly mixed the batches while maintaining separation between layers (Figure 3D). Notably, batch-specific clusters were no longer present within individual layers. Our test showed that by combining SEDR with Harmony, we were able to effectively remove the batch effects present. Among the other spatial omics analysis methods, only stLearn produces a latent space embedding which can be fed to Harmony for batch correction, therefore we benchmarked SEDR against stLearn. As stLearn is unable to jointly project different batches to a shared latent space due to its requirement of histological images as input, we generated a latent space embedding from each dataset and then concatenated them for Harmony integration. The results showed that batches were not well mixed, and the layers were poorly separated (Figure 3E). In conclusion, SEDR combined with Harmony outperforms both Harmony alone and stLearn with Harmony, and this

can serve as an effective method for batch correction of spatial omics data.

Dissecting tumor heterogeneity and immune microenvironment using SEDR.

Intratumor heterogeneity in cancer complicates effective treatment formulations and is associated with poor survival prospects[35]. Spatial transcriptomics is an effective tool for meeting the challenge to dissect and characterize intratumor heterogeneity and tumor-immune crosstalk. Here, we tested SEDR on the 10x Visium spatial transcriptomic data of human breast cancer, which is known for its high intratumoral and intertumoral differences. To aid the interpretation of SEDR results, we performed manual pathology labeling based on the H&E staining. It should be noted that unlike the cerebral cortex that has clear and established morphological boundaries, tumor tissues are highly heterogeneous and encompass complex tumor microenvironments. Manual labeling solely based on tumor morphology is inadequate to characterize such complexity. Based on pathological features, we manually segmented the histological image into 20 regions and grouped them into 4 main morphotypes: Ductal Carcinoma *in Situ*/Lobular Carcinoma *in Situ* (DCIS/LCIS), healthy tissue (Healthy), Invasive Ductal Carcinoma (IDC), and tumor surrounding regions with low features of malignancy (Tumor edge) (Figure 4A). Visually, all five clustering methods agree with the manual annotation at the macroscopic level. Nevertheless, the SEDR clusters presented a smoother segmentation compared to other methods, while Seurat, stLearn and SpaGCN derived clusters appear fragmented and have irregular boundaries. Notably, SEDR found more sub-clusters within the tumor regions, while other methods were prone to divide the healthy regions into sub-clusters, given that all methods were set to generate the same number of clusters. For instance, within DCIS/LCIS_3, SEDR separated an outer “ring” (cluster 7) from the tumor core (cluster 3), and partitioned IDC_2 into 3 sub-clusters. These SEDR sub-clusters suggested transcriptomic heterogeneity within the seemly homogeneous tumor regions. In addition to clustering analysis, we also employed Seurat3 ‘anchor’-based integration workflow to perform probabilistic transfer of annotations from a reference scRNA-seq data of human breast cancer[36] to the spatial data and output, for each spot, a probabilistic classification for each of

the scRNA-seq derived classes (Figure 4B, Supplementary Figure 1). The transferred class probabilities were able to delineate the tumor regions and regions where immune cells or fibroblasts were present, which will aid in further dissecting the tumor micro-environment.

A number of driving forces have been hypothesized for the metastatic transition of tumor cells from a pre-invasive state to invasive carcinoma, including pro-tumor immune microenvironment and reduced cell-cell interactions within the tumor[37]. Here, we employed PAGA to infer the inter-relatedness between the manually annotated DCIS/LCIS and IDC regions in an attempt to trace the metastatic transition process. The PAGA graph generated using the SEDR embedding showed that DCIS_LCIS_3 was the only DCIS/LCIS region that was likely to spread to its neighboring invasive tumor region IDC_6 (Figure 4C). DEGs between DCIS_LCIS_3 and all other DCIS_LCIS regions and enriched pathways showed that DCIS_LCIS_3 had more immune infiltrates (Supplementary Figure 2A, 2B, 2C), in particular tumor associated macrophages (TAM) (Figure 4B, Supplementary Figure 2D), while the other DCIS_LCIS regions were mainly comprised of epithelial cells that were actively dividing / cycling (Figure 4B) and had up-regulated glycolytic and metabolic processes (Supplementary Figure 2C). TAM infiltration is known to strongly associate with poor survival in solid tumor patients by promoting tumor angiogenesis and inducing tumor migration, invasion and metastasis[38,39]. We then performed Monocle3 analysis to infer the pseudo-time of the transition from DCIS_LCIS_3 to IDC_6. As DCIS_LCIS_3 and IDC_6 coincide with SEDR clusters 3, 7, and 11 (Figure 4A), we performed Monocle3 on these three clusters and set cluster 3 as the starting point (Figure 4C bottom). We subsequently identified genes that changed expression along Monocle3 pseudotime and revealed sequential waves of gene regulation along the trajectory (Figure 4D). As SEDR cluster 3 and 7 marked the core and outer ring of DCIS/LCIS_3, we identified genes differentially expressed between these two clusters and enriched pathways to further dissect intratumoral heterogeneity (Figure 4E). In cluster 3, we observed the up-regulation of interferon signaling pathways (IFIT1, IFITM1,

IFITM3 and TAP1) and NK or neutrophil activities (FCGR3B and TNFSF10) (Figure 4E, Supplementary Figure 2E). In addition, upregulation of RHOB in this region points towards reduced metastatic potential[40]. Cluster 3 represents a region where cancer growth was limited by pro-inflammatory immune responses. On the other hand, in cluster 7, we observed the presence of TAMs (Figure 4B), memory B cells (IGHG1, IGHG3, IGHG4, IGLC2 and IGLC3) and fibroblasts (COL1A1, COL1A2, COL3A1, COL5A1, COL6A1, COL6A2 and FN1) (Figure 4E, Supplementary Figure 2E). Upregulated cathepsin activities (CTSB, CTSD and CTSZ) and complement pathway (C1QA, C1S and C4) indicate pro-tumor activities by the TAMs in this region[41,42,43]. Moreover, upregulated cathepsin activity and metalloprotease inhibitors (TIMP1 and TIMP3) also suggests disturbance in extracellular matrix integrity. Overall, cluster 7 represents a region with an immune-suppressed pro-tumor microenvironment and had high potential of cancer metastasis. In summary, SEDR analysis led to the identification of a potentially invasive DCIS region: DCIS/LCIS_3, where the outer ring cluster 7 had TAM infiltration and cancer associated fibroblasts (CAFs) presence, of which both have been reported to facilitate tumor spread[44,45]. SEDR also enabled the mapping of a molecular path or trajectory from DCIS to IDC. Taken together, SEDR can help dissect intratumoral heterogeneity and understand the relationships between different tumor compartments.

SEDR can handle spatial transcriptomics data with high resolution.

Currently available spatial omics technologies including 10x Visium Spatial Omics, Nanostring GeoMX DSP, SLIDE-seq[4], and DBIT-seq[46], do not have single-cell resolution with each capture spot containing 1 to 10 cells. Meanwhile, new emerging methods such as Stereo-seq[5], PIXEL-Seq[6] and Seq-Scope[7] can achieve submicrometer and thus subcellular resolution. With continued advances of spatial omics technologies, spatial resolution and number of cells detected per tissue will significantly improve, producing big datasets with high throughput. Here, we evaluated SEDR's performance on one type of such data (Stereo-seq) of mouse olfactory bulb (Figure 5). Coronal section of the mouse olfactory bulb shows the olfactory nerve layer (ONL), glomerular layer (GL), external plexiform layer (EPL), mitral cell layer (MCL),

283 internal plexiform layer (IPL), granule cell layer (GCL) and rostral migratory stream (RMS)
284 (Figure 5A). We performed unsupervised clustering using Seurat-derived principal
285 components and SEDR-derived embedding to computationally reconstruct the spatial identity
286 of the olfactory bulb profiled with Stereo-seq. Compared to Seurat clusters, SEDR clusters
287 better reflected tissue organization and were more consistent with known anatomical layers
288 (Figure 5B, 5C). We also performed quantitative assessment using local inverse Simpson's
289 index (LISI) and found SEDR produced significantly lower LISI than Seurat showing SEDR
290 clusters were better spatially separated.

291

292 ## Discussion

293 Cell type heterogeneity is a feature of tissue, both healthy and diseased. Capturing this
294 heterogeneity, coupled with their spatial arrangement in the tissue, is crucial when studying
295 the roles of these cells and their cross-talk. Spatial omics technologies represent the state-of-
296 the-art approach to capture omics data with corresponding spatial information from tissue
297 samples. We present SEDR, which leverages on cutting edge machine learning techniques
298 to achieve a better representation of spatial omics data that can be used for clustering and
299 further downstream analyses. SEDR first learns a low dimension latent space representation
300 of the transcriptome information with a deep autoencoder network, which is then aggregated
301 with spatial neighbor information by a variational graph autoencoder to create a spatial
302 embedding. This spatial embedding is then concatenated with the gene expression to be
303 decoded to reconstruct the final gene expression for further analyses. We first demonstrated
304 its efficacy in delineating the different cerebral cortex layers with higher clarity than competing
305 methods, and recapitulated the associated development order by using the joint latent
306 representation with Monocle3.

307 To enhance the analytical power and resolution of spatial omics, we need to integrate multiple
308 datasets from the same tissue. Similar to single-cell transcriptomic data, spatial omics datasets
309 generated in different batches also contain batch-specific systematic variations that present a

challenge to batch-effect removal and data integration. In our study, we demonstrated that by combining SEDR and Harmony, we were able to effectively remove batch effects present. In the future, we will integrate Harmony into the SEDR workflow.

Spatial omics technologies such as Stero-seq are able to measure large number of cells per experiment through high spatial resolution and large tissue sizes. In the near future, we expect to see ever increasing throughput from spatial omics experiments, which will result in spatial omics big data that pose significant challenges to data analysis and integration. Computational methods that employ graph neural network require loading the entire graph into GPU memory, which inhibits their applications to very large datasets. We will improve the memory efficiency of SEDR by using GCN min-batch or parallel techniques to construct large-scale graphs for spatial omics data of high throughput and high resolution. Furthermore, technologies with capture spot size smaller than the size of a cell will also require new computational methods that can accurately delineate cells based on capture spots. In the future, we will integrate cell segmentation based on H&E or DAPI staining into SEDR workflow.

The current SEDR methodology focuses on gene expression and spatial information, and does not make use of histological images. Contemporary methods such as SpaGCN and stLearn use histological images as input, but in a suboptimal fashion, as demonstrated in our study. SpaGCN utilizes histological image pixels as features by calculating the mean color value from the RGB channels directly. However, the pixel values are easily affected by noise and cannot provide a semantic feature for cell analysis. A more effective approach could be adopting deep CNN model which can learn a high-level representation for histological image. stLearn introduces a deep learning model to extract image features of the spots, and integrates them with the spatial location and gene expression. However, stLearn employs a pre-model trained based on natural images, and does not fine-tune the network towards histological images. In the future, we will incorporate histological images as an additional modality into the SEDR model. We will utilize an image autoencoder network to learn image features, and jointly learn the latent representation by integrating gene expression, image morphology, and spatial

information.

In summary, SEDR is a promising new approach that builds an integrated representation of cells using both transcriptomic data and spatial coordinates. SEDR derived low dimensional embedding enables more accurate clustering, trajectory inference and batch effect correction. It is able to handle both spatial transcriptomics with capture spot sizes ranging from 50um to less than 1um. Application of SEDR on human breast cancer revealed heterogeneous sub-regions within seemly homogenous tumor regions and shed light on the role of immune microenvironment on tumor invasiveness.

Methods

Dataset preprocessing.

Our SEDR method takes spatial transcriptomics gene expression and spatial coordinates as inputs. The raw gene expression counts are first normalized using the respective library sizes (by normalize_total in Scanpy (v.1.5.0)), with very highly expressed genes excluded from the computation of the normalization factor (size factor) for each cell[47]. Principal component analysis (PCA) is then performed to extract the first 300 principal components to generate the initial gene expression matrix.

Graph construction for spatial transcriptomics data.

To create the graph representing the cell–cell spatial relationships of spatial transcriptomics data, we calculated the Euclidean distance in the image coordinates of all cells and selected the top 10 nearest neighbors of each cell to construction the adjacency matrix. The adjacency matrix, denoted by A, is a symmetric matrix, where $A_{ij} = A_{ji} = 1$ if i and j are neighbors, and 0 otherwise.

Deep autoencoder for latent representation learning.

The latent representation of the gene expression is learned through a deep autoencoder. The encoder part, consisting of two fully connected stacked layers, generates the low-dimensional representation $Z_f \in \mathbb{R}^{N\times D_f}$ from the input gene expression matrix $X \in \mathbb{R}^{N\times M}$, while the decoder part with one fully connected layer, reconstructs the expression $X' \in \mathbb{R}^{N\times M}$ from the latent representation $Z \in \mathbb{R}^{N\times D}$, which is obtained by concatenating the low-dimensional representation Z_f and spatial embedding $Z_g \in \mathbb{R}^{M\times D_g}$, where N is the number of cell, M is the number of input genes, and D_f, D_g, D are the dimensions of the learned low-dimensional expression representation of encoder, spatial embedding of GCN, and final latent representation of SEDR with $D = D_f + D_g$. The objective function of the deep autoencoder maximizes the similarity between the input gene and reconstructed expressions, as measured

by the mean squared error (MSE) loss function, $\sum(X - X')^2$.

Variational graph autoencoder for spatial embedding.

SEDR utilizes a variational graph autoencoder[48] (VGAE) to embed the spatial information of neighborhood cells. With the adjacency matrix A and its degree matrix D, the VGAE learns a graph embedding Z_g with the formal format as: $g: (A, Z_f) \longrightarrow Z_g$, where Z_f is the node/gene representation from the deep autoencoder. The inference part of VGAE is parameterized by a two-layer graph convolutional network[49] (GCN):

$$g(Z_g|A, Z_f) = \prod g(z_i|A, Z_f), \text{ with } g(z_i|A, Z_f) = \mathcal{N}(z_i|\mu_i, diag(\sigma_i^2)),$$

where $\mu = GCN_\mu(A, Z_f)$ is the matrix of mean vectors, and $log\sigma = GCN_\sigma(A, Z_f)$. The two-layer GCN is defined as $GCN(A, Z_f) = \tilde{A}\, ReLU(\tilde{A}Z_f W_0)W_1$, with weight W_i and symmetrically normalized adjacency matrix $\tilde{A} = D^{-\frac{1}{2}}AD^{-\frac{1}{2}}$. The spatial embedding Z_g and reconstructed adjacency matrix A' are generated as:

$$A' = \sigma(Z_g \cdot Z_g^T), \text{ with } Z_g = GCN\ (A, Z_g).$$

The objective function of the VGAE is to minimize the cross-entropy (CE) loss between input adjacency matrix A and reconstructed adjacency matrix A', and simultaneously, minimize Kullback-Leibler (KL) divergence between $g(Z_g|A, Z_f)$ and Gaussian prior $p(Z_g) = \prod_i \mathcal{N}(z_i|0, I)$.

Batch effect correction for spatial transcriptomics

The spatial relationship only exists within single spatial omics, and the cells from different omics have no direct spatial relation. Let the A^k and Z_f^k denotes the adjacency matrix and deep gene representation of spatial omics k, we could create a block-diagonal adjacency matrix A^k and concatenate the deep gene representation in the cell dimension, as:

$$A = \begin{bmatrix} A^1 & \cdots & 0 \\ \vdots & \ddots & \vdots \\ 0 & \cdots & A^K \end{bmatrix}, \quad Z_f = \begin{bmatrix} Z_f^1 \\ \vdots \\ Z_f^K \end{bmatrix},$$

where K is the number of spatial omics. Based on this, we could feed different spatial omics (of potentially different size) as multiple graph instances in the form of one block-diagonal adjacency matrix to the SEDR.

For removing batch effects and enhancing the compactness of its latent representation, SEDR employs an unsupervised deep embedded clustering (DEC) method[26] to iteratively group the cells into different clusters. To initialize the cluster centers, we employ the KMeans of scikit-learn on the learned latent representations. The number of clusters is pre-defined as a hyper-parameter. With the initialization, the DEC improves the clustering using an unsupervised iterative method with two steps. In the first step, a soft assignment q_{ij} between the cluster center μ_j and latent point z_i is calculated by Student's t-distribution, as:

$$q_{ij} = \frac{\left(1+\left||z_i-\mu_j|\right|^2\right)^{-1}}{\sum_{j'}\left(1+\left||z_i-\mu_{j'}|\right|^2\right)^{-1}}.$$

In the second step, we iteratively refine the clusters by learning from their high confidence assignments with the help of an auxiliary target distribution P based on q_{ij}, as:

$$p_{ij} = \frac{q_{ij}^2/\sum_i q_{ij}}{\sum_{j'}(q_{ij'}^2/\sum_i q_{ij'})}.$$

Based on the soft assignment q_{ij} and auxiliary target distribution p_{ij}, an objective function is defined using the KL divergence:

$$KL(P||Q) = \sum_i \sum_j p_{ij} \log \frac{p_{ij}}{q_{ij}}.$$

The SEDR parameters and cluster centers are then simultaneously optimized by using stochastic gradient descent (SGD) with momentum.

Seurat.

Raw mRNA counts were preprocessed to remove low quality genes and sctransformed to remove technical artifacts and normalize the data[50]. We then ran Principal Component

Analyses (PCA) to extract the top 30 Principal Components (PCs) and use them to calculate the shared nearest neighbors (SNN). Then the Louvain clustering algorithm was used to identify clusters with the SNN networks. We tried clustering at different resolutions to obtain the same number of clusters as the number of ground truth layers.

SpaGCN, stLearn, BayesSpace, Giotto.

We ran these methods with recommended pipelines and defualt parameters and set each method to generate the same number of clusters as the number of ground truth layers. stLearn-derived low dimensional embedding was used to for downstream UMAP visualization and harmony batch correction.

Evaluation metric for clustering.

For datasets with cell-type labels (e.g., DLPFC), we employed the adjusted rand index (ARI) to compare the performance of different clustering algorithms. The index calculates the similarity between the clustering labels predicted by algorithm and reference cluster labels as:

$$ARI = \frac{RI - E[RI]}{\max(RI) - E[RI]},$$

where the unadjusted rand index (RI) is defined as: $RI = (a + b)/C_n^2$, with a as the number of pairs correctly labeled in the same sets, b as the number of pairs correctly labeled as not in the same data set, and C_n^2 as the total number of possible pairs. $E[RI]$ is the expected RI of random labeling. A higher ARI score indicates better performance.

Monocle3.

On DLPFC #151673 slice and breast cancer data, we ran Monocle3 using both Seurat and SEDR outputs. For Seurat, we ran the standard pipeline to get UMAP and used UMAP as input for Monocle3. For SEDR, we first extracted SEDR low dimensional embedding and then used uwot package to calculate UMAP. We then ran Monocle3 on both UMAP using recommended parameters and set white matter (WM) as the start point to generate pseudotime. We then used Moran_I test for detecting significant genes that showed correlation with pseudotime.

Leiden clustering, PAGA trajectory, and UMAP for comparison.

The Leiden clustering, partition-based graph abstraction (PAGA), and uniform manifold approximation and projection (UMAP) of the gene representation and spatial embeddings/principal components (PCs) derived from the SEDR and Seurat were performed using Scanpy (v.1.5.0) package. Briefly, all embeddings or first 30 PCs were directly used to compute a neighborhood graph of observations using n_neighbors of 15, UMAP method to compute the connectivities, and Euclidean method to compute the distance. In order to obtain the same amount of unique Leiden clusters obtained using the SEDR, grid-searching on the Leiden clustering resolution between 0.2 and 2.5 with interval of 0.05/0.01 were performed. Subsequently, the PAGA was performed to quantify the connectivity of Leiden clusters. Lastly, the cluster positions suggested by PAGA were used to initialize the UMAP manifold learning for visualization.

Harmony.

Harmony was used to correct batch effect on low dimensional embeddings. For SEDR, we used latent space embeddings as input. For raw data and stLearn, we used the PCA embeddings as input. We treated different samples as different batches and set all other parameters with default value. For each method, the uncorrected embeddings and batch corrected Harmony embeddings were used to do UMAP analysis.

Prediction of cell type composition of 10x Visium spatial spot.

We downloaded a published scRNA-seq dataset of human breast cancer[36] as reference, and ran Seurat to find transfer anchors between the reference and our Visium spatial data. Cell types in the reference are then assigned to the spatial spots by label transferring. We removed cell types that have probability equal to 0 for all spots.

Differential Expression Genes (DEGs) and pathway analyses.

We use Seurat to identify DEGs. Genes with adjusted p-value < 0.05 is used as the input for QIANGEN Ingenuity Pathway Analysis (IPA). For IPA result, the pathway with positive or

negative z-score are plotted.

Raw data processing of Stereo-seq data.

Fastq files were generated using MGI DNBSEQ-Tx sequencer. Coordinate identity (CID) and unique molecular identifier (UMI) are contained in the forward reads (CID: 1-25bp, UMI: 26-35bp) while the reverse reads consist of the cDNA sequences. CID sequences on the forward reads were first mapped to the designed coordinates of the *in situ* captured chip, allowing 1 base mismatch to correct for sequencing and PCR errors. Reads with UMI containing either N bases or more than 2 bases with quality score lower than 10 were filtered out. CID and UMI associated with each read were appended to each read header. Retained reads were then aligned to the reference genome (mm10) using STAR[51] and mapped reads with MAPQ ≥10 were counted and annotated to their corresponding genes using an *in-house* script (available at https://github.com/BGIResearch/handleBam). UMI with the same CID and the same gene locus were collapsed, allowing 1 mismatch to correct for sequencing and PCR errors. Finally, this information was used to generate a CID-containing expression profile matrix.

Local inverse Simpson's index (LISI).

We first used Seurat and SEDR to generate cell clusters for the stereo-seq data, then used R "lisi" package to calculate LISI with coordinates as X and clustering results of Seurat and SEDR as meta data.

Data availability.

(1) The LIBD human dorsolateral prefrontal cortex (DLPFC) Data (http://spatial.libd.org/spatialLIBD/);

Software availability.

SEDR is written by Python using the PyTorch library. An open-source implementation of SEDR

492 is released on https://github.com/HzFu/SEDR

493

494

495

496

References

1. Ståhl, P. L. *et al.* Visualization and analysis of gene expression in tissue sections by spatial transcriptomics. *Science* (2016) doi:10.1126/science.aaf2403.
2. Maynard, K. R. *et al.* Transcriptome-scale spatial gene expression in the human dorsolateral prefrontal cortex. *Nat. Neurosci.* **24**, 425–436 (2021).
3. Ji, A. L. *et al.* Multimodal Analysis of Composition and Spatial Architecture in Human Squamous Cell Carcinoma. *Cell* (2020) doi:10.1016/j.cell.2020.08.043.
4. Rodriques, S. G. *et al.* Slide-seq: A scalable technology for measuring genome-wide expression at high spatial resolution. *Science (80-.).* (2019) doi:10.1126/science.aaw1219.
5. Chen, A. *et al.* Large field of view-spatially resolved transcriptomics at nanoscale resolution Short title: DNA nanoball stereo-sequencing. *bioRxiv* 2021.01.17.427004 (2021).
6. Fu, X. *et al.* Continuous Polony Gels for Tissue Mapping with High Resolution and RNA Capture Efficiency. *bioRxiv* 2021.03.17.435795 (2021).
7. Cho, C.-S. *et al.* Seq-Scope: Submicrometer-resolution spatial transcriptomics for single cell and subcellular studies. *bioRxiv* (2021).
8. Stickels, R. R. *et al.* Highly sensitive spatial transcriptomics at near-cellular resolution with Slide-seqV2. *Nat. Biotechnol.* (2021) doi:10.1038/s41587-020-0739-1.
9. Liu, Y. *et al.* High-Spatial-Resolution Multi-Omics Sequencing via Deterministic Barcoding in Tissue. *Cell* (2020) doi:10.1016/j.cell.2020.10.026.
10. Lein, E., Borm, L. E. & Linnarsson, S. The promise of spatial transcriptomics for neuroscience in the era of molecular cell typing. *Science* (2017) doi:10.1126/science.aan6827.
11. Yoosuf, N., Navarro, J. F., Salmén, F., Ståhl, P. L. & Daub, C. O. Identification and transfer of spatial transcriptomics signatures for cancer diagnosis. *Breast Cancer Res.* (2020) doi:10.1186/s13058-019-1242-9.

12. van den Brink, S. C. *et al.* Single-cell and spatial transcriptomics reveal somitogenesis in gastruloids. *Nature* (2020) doi:10.1038/s41586-020-2024-3.

13. Dong, R. & Yuan, G. C. SpatialDWLS: accurate deconvolution of spatial transcriptomic data. *Genome Biol.* **22**, 1–10 (2021).

14. Song, Q. & Su, J. DSTG: deconvoluting spatial transcriptomics data through graph-based artificial intelligence. *Brief. Bioinform.* (2021) doi:10.1093/bib/bbaa414.

15. Andersson, A. *et al.* Single-cell and spatial transcriptomics enables probabilistic inference of cell type topography. *Commun. Biol.* **3**, 1–8 (2020).

16. Biancalani, T. *et al.* Deep learning and alignment of spatially-resolved whole transcriptomes of single cells in the mouse brain with Tangram. *bioRxiv* (2020).

17. Gayoso, A. *et al.* scvi-tools: a library for deep probabilistic analysis of single-cell omics data. *bioRxiv* (2021).

18. Lopez, R. *et al.* Multi-resolution deconvolution of spatial transcriptomics data reveals continuous patterns of inflammation. *bioRxiv* (2021).

19. Elosua-Bayes, M., Nieto, P., Mereu, E., Gut, I. & Heyn, H. SPOTlight: seeded NMF regression to deconvolute spatial transcriptomics spots with single-cell transcriptomes. *Nucleic Acids Res.* (2021) doi:10.1093/nar/gkab043.

20. Danaher, P. *et al.* Advances in mixed cell deconvolution enable quantification of cell types in spatially-resolved gene expression data. *bioRxiv* (2020).

21. Hao, Y. *et al.* Integrated analysis of multimodal single-cell data. *Bioarxiv* (2020).

22. Zhao, E. *et al.* Bayesspace enables the robust characterization of spatial gene expression architecture in tissue sections at increased resolution. *bioRxiv* (2020) doi:10.1101/2020.09.04.283812.

23. Dries, R. *et al.* Giotto: a toolbox for integrative analysis and visualization of spatial expression data. *Genome Biol.* **22**, 78 (2021).

24. Hu, J. *et al.* Integrating gene expression, spatial location and histology to identify spatial 1 domains and spatially variable genes by graph convolutional network 2 3. *bioRxiv* 2020.11.30.405118 (2020).

552 25. Pham, D. *et al.* stLearn: Integrating spatial location, tissue morphology and gene
553 expression to find cell types, cell-cell interactions and spatial trajectories within
554 undissociated tissues. *bioRxiv* (2020) doi:10.1101/2020.05.31.125658.
555 26. Xie, J., Girshick, R. & Farhadi, A. Unsupervised Deep Embedding for Clustering
556 Analysis. in *ICML* (eds. Balcan, M. F. & Weinberger, K. Q.) vol. 48 478–487 (PMLR,
557 2016).
558 27. Mann, H. B. & Whitney, D. R. On a Test of Whether one of Two Random Variables is
559 Stochastically Larger than the Other. *Ann. Math. Stat.* **18**, 50–60 (1947).
560 28. Trapnell, C. *et al.* The dynamics and regulators of cell fate decisions are revealed by
561 pseudotemporal ordering of single cells. *Nat. Biotechnol.* **32**, 381–386 (2014).
562 29. Cao, J. *et al.* The single-cell transcriptional landscape of mammalian organogenesis.
563 *Nature* **566**, 496–502 (2019).
564 30. Wolf, F. A. *et al.* PAGA: graph abstraction reconciles clustering with trajectory
565 inference through a topology preserving map of single cells. *Genome Biol.* **20**, 1–9
566 (2019).
567 31. Gilmore, E. G. & Herrup, K. Cortical development: Layers of complexity. *Current*
568 *Biology* (1997) doi:10.1016/s0960-9822(06)00108-4.
569 32. Chini, M. & Hanganu-Opatz, I. L. Prefrontal Cortex Development in Health and
570 Disease: Lessons from Rodents and Humans. *Trends in Neurosciences* (2021)
571 doi:10.1016/j.tins.2020.10.017.
572 33. Nadarajah, B. & Parnavelas, J. G. Modes of neuronal migration in the developing
573 cerebral cortex. *Nature Reviews Neuroscience* (2002) doi:10.1038/nrn845.
574 34. Tran, H. T. N. *et al.* A benchmark of batch-effect correction methods for single-cell
575 RNA sequencing data. *Genome Biol.* (2020) doi:10.1186/s13059-019-1850-9.
576 35. Nguyen, P. H. D. *et al.* Intratumoural immune heterogeneity as a hallmark of tumour
577 evolution and progression in hepatocellular carcinoma. *Nat. Commun.* **12**, 1–13
578 (2021).
579 36. *et al.* A single-cell RNA expression atlas of normal, preneoplastic and tumorigenic

states in the human breast. *EMBO J.* **40**, 1–23 (2021).

37. Friedl, P. & Alexander, S. Cancer invasion and the microenvironment: Plasticity and reciprocity. *Cell* (2011) doi:10.1016/j.cell.2011.11.016.

38. Kuroda, H. *et al.* Tumor microenvironment in triple-negative breast cancer: the correlation of tumor-associated macrophages and tumor-infiltrating lymphocytes. *Clin. Transl. Oncol.* (2021) doi:10.1007/s12094-021-02652-3.

39. Asiry, S. *et al.* The Cancer Cell Dissemination Machinery as an Immunosuppressive Niche: A New Obstacle Towards the Era of Cancer Immunotherapy. *Front. Immunol.* **12**, 1–19 (2021).

40. Ju, J. A., Godet, I., DiGiacomo, J. W. & Gilkes, D. M. RhoB is regulated by hypoxia and modulates metastasis in breast cancer. *Cancer Rep.* (2020) doi:10.1002/cnr2.1164.

41. Olson, O. C. & Joyce, J. A. Cysteine cathepsin proteases: Regulators of cancer progression and therapeutic response. *Nature Reviews Cancer* (2015) doi:10.1038/nrc4027.

42. Roumenina, L. T. *et al.* Tumor cells hijack macrophage-produced complement C1q to promote tumor growth. *Cancer Immunol. Res.* (2019) doi:10.1158/2326-6066.CIR-18-0891.

43. Fraser, D., Melzer, E., Camacho, A. & Gomez, M. Macrophage production of innate immune protein C1q is associated with M2 polarization (INM1P.434). *J. Immunol.* (2015).

44. Monteran, L. & Erez, N. The dark side of fibroblasts: Cancer-associated fibroblasts as mediators of immunosuppression in the tumor microenvironment. *Frontiers in Immunology* (2019) doi:10.3389/fimmu.2019.01835.

45. Lin, Y., Xu, J. & Lan, H. Tumor-associated macrophages in tumor metastasis: Biological roles and clinical therapeutic applications. *Journal of Hematology and Oncology* (2019) doi:10.1186/s13045-019-0760-3.

46. Deng, Y. *et al.* Resource High-Spatial-Resolution Multi-Omics Sequencing via

608 Deterministic Barcoding in Tissue ll ll Resource High-Spatial-Resolution Multi-Omics
609 Sequencing via Deterministic Barcoding in Tissue. *Cell* **183**, 1665-1681.e18 (2020).
610 47. Weinreb, C., Wolock, S. & Klein, A. M. SPRING: a kinetic interface for visualizing high
611 dimensional single-cell expression data. *Bioinformatics* **34**, 1246–1248 (2018).
612 48. Kipf, T. N. & Welling, M. Variational Graph Auto-Encoders. in *NIPS Workshop on*
613 *Bayesian Deep Learning* (2016).
614 49. Kipf, T. N. & Welling, M. Semi-Supervised Classification with Graph Convolutional
615 Networks. in *International Conference on Learning Representations (ICLR)* (2017).
616 50. Hafemeister, C. & Satija, R. Normalization and variance stabilization of single-cell
617 RNA-seq data using regularized negative binomial regression. *Genome Biol.* **20**, 296
618 (2019).
619 51. Dobin, A. *et al.* STAR: Ultrafast universal RNA-seq aligner. *Bioinformatics* (2013)
620 doi:10.1093/bioinformatics/bts635.
621
622

Acknowledgements:

This research was supported by funding from Singapore Immunology Network (SIgN), A * STAR, Singapore.

Author contributions:

Huazhu Fu designed and implemented SEDR. Hang Xu, Huazhu Fu, Kelvin Chong, Mengwei Li, Hong Kai Lee and Jingjing Ling performed data analysis. Hang Xu, Huazhu Fu, Mengwei Li generated figures. Jinmiao Chen, Huazhu Fu, Hang Xu, Kok Siong Ang, Kelvin Chong, Jingjing Ling and Ling Shao drafted the manuscript. Ao Chen and Longqi Liu provided Stereo-seq data. Jinmiao Chen conceptualized and supervised the study.

Competing interests:

The authors declare no competing interests.

Figure legend:

Figure 1. Overview of SEDR. SEDR learns a low-dimensional latent representation of gene expression embedded with spatial information via jointly training a deep autoencoder and a variational graph autoencoder. The low dimensional embedding produced by SEDR can be used for downstream visualization, cell clustering, trajectory inference and batch effect correction.

Figure 2. Quantitative assessment of SEDR on human dorsolateral prefrontal cortex (DLPFC) dataset. A) Ground-truth segmentation of cortical layers; clustering results of Seurat, Giotto, stLearn, SpaGCN, BayesSpace and SEDR on DLPFC slice #151673; Adjusted rand index (ARI) of various cluster sets on 12 DLPFC slices. B) UMAP visualization and Monocle trajectory generated using Seurat-derived PCA embedding (top) and SEDR embedding (bottom); Monocle pseudotimes were visualized on UMAP plot and spatial co-ordinates. C) PAGA graph generated using Seurat-derived PCA embedding and SEDR embedding; SEDR showed a higher percentage of weights of correct PAGA edges compared to Seurat.

Figure 3. Batch effect present in DLPFC datasets and assessment of SEDR's performance on batch correction. A) The slices #151507, #151672 and #151673 showed substantial inter-slice variations before batch effect correction. UMAP plots colored by ground-truth cortical layers (left), slices (right), split by slices and colored by layers (bottom). B) Harmony alone was unable to remove the batch effects present. C) SEDR alone substantially reduced batch effects. D) SEDR combined with Harmony effectively corrected for batch effects. E) stLearn combined with Harmony was unable to correct for batch effects.

Figure 4. Application of SEDR on 10x Visium spatial transcriptomics data of human breast cancer. A) Manual pathology labeling based on the H&E staining; clustering results of SEDR, Seurat, stLearn, SpaGCN and BayesSpace. B) Seurat3 'anchor'-based integration workflow was used to perform probabilistic transfer of annotations from a reference scRNA-seq data of human breast cancer to the spatial data and output, for each spot, a probabilistic classification for each of the scRNA-seq derived classes. The probabilities of tumor associated macrophage (TAM) and cycling epithelial (C.Epi) were visualized. C) Trajectory analysis results using PAGA (Top) and Monocle3 (Bottom). PAGA graph predicted the inter-relatedness between the manually annotated DCIS/LCIS and IDC regions. Edge width, a measure of connectivity strength, indicates the likelihood of an actual connection being present. Monocle3 inferred pseudotimes of spots in SEDR cluster 3, 7 and 11 using Seurat-derived PCA embedding (termed "rna_pseudotime") and SEDR embedding (termed "SEDR_pseudotime"). D) Heatmap of genes whose expression changed along Monocle-derived pseudotime. E) Pathways enriched by genes differentially expressed between SEDR cluster 3 and 7. Red bars represent pathways up-regulated in cluster 3.

Figure 5. Application of SEDR on Stereo-seq spatial transcriptomics data of mouse olfactory bulb tissue section. A) Laminar organization of DAPI stained mouse olfactory bulb. B) Unsupervised clustering of the spatial voxels analyzed by Seurat and SEDR. C) Four clusters with the highest number of voxels were selected and visualized. D) Quantitative comparison of Seurat and SEDR clusters using local inverse Simpson's index (LISI).

677 **Supplementary:**

678 Figure 1. **Complete deconvolution result for breast cancer sample.**

679 Figure 2. **Differential expression genes and enriched pathways.** A) Position of
680 DCIS_LCIS_3 and other DCIS_LCIS regions. B) Top DEGs between DCIS_LCIS_3 and other
681 DCIS_LCIS regions. C) Enriched pathways of DEGS for DCIS_LCIS_3 vs other DCIS_LCIS
682 regions. D) Percentage of TAM for cluster 3 and cluster 7 of SEDR clustering result. E)
683 Representative DEGs between cluster 3 and cluster 7.

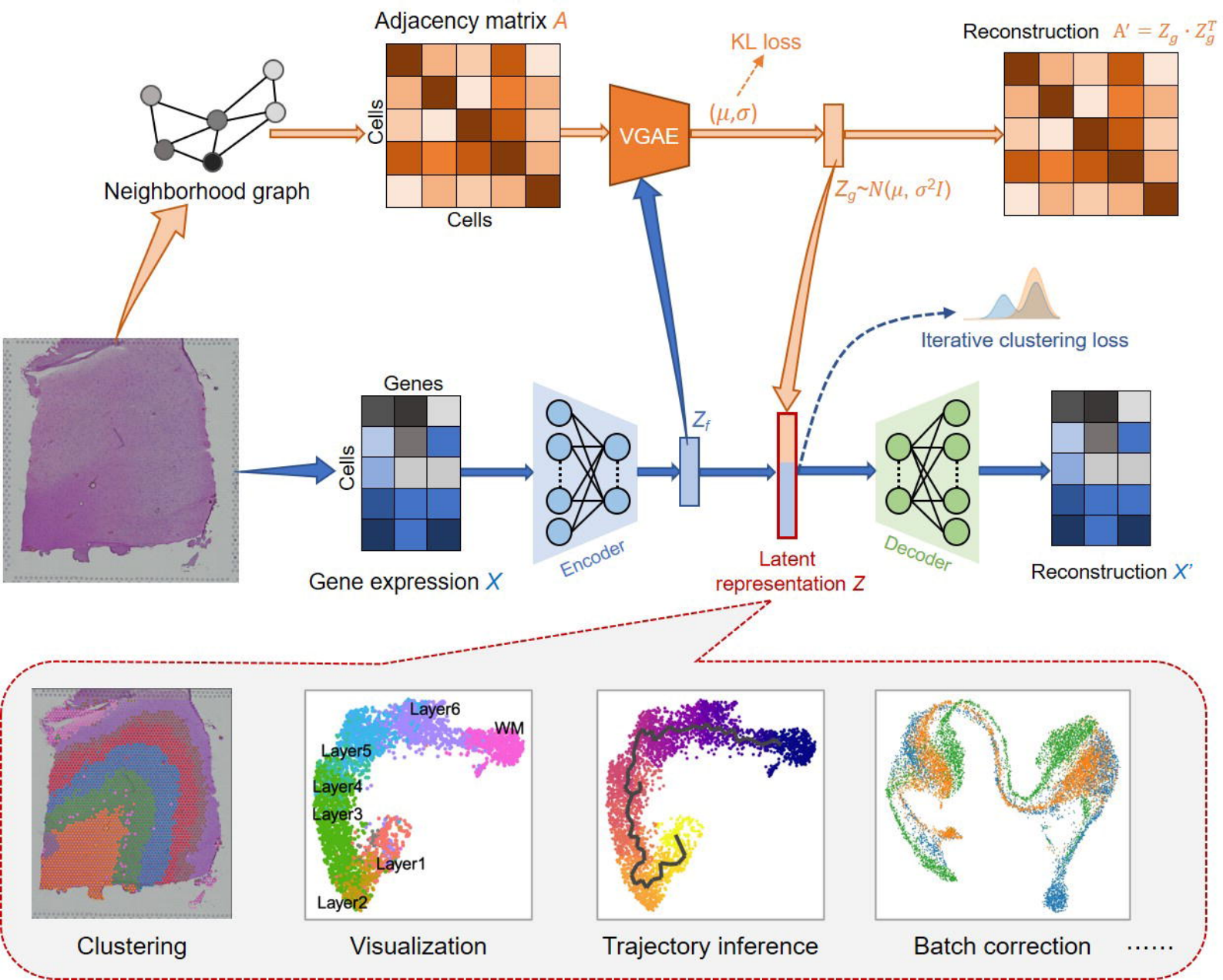
Adjacency matrix A
Cells
Cells
Neighborhood graph
VGAE
KL loss
(μ,σ)
$Z_g \sim N(\mu, \sigma^2 I)$
Reconstruction $A' = Z_g \cdot Z_g^T$
Iterative clustering loss
Genes
Cells
Gene expression X
Encoder
Z_f
Latent representation Z
Decoder
Reconstruction X'
Layer6
WM
Layer5
Layer4
Layer3
Layer1
Layer2
Clustering
Visualization
Trajectory inference
Batch correction
.....

A

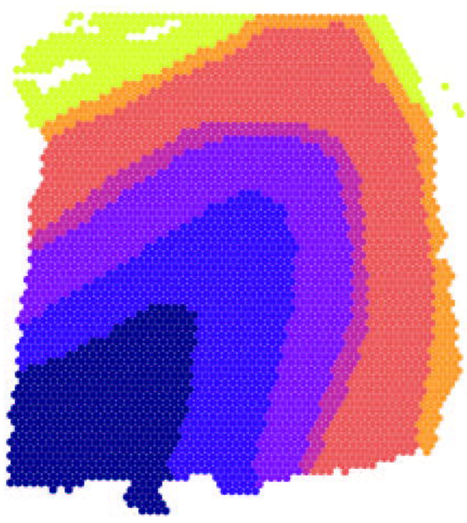

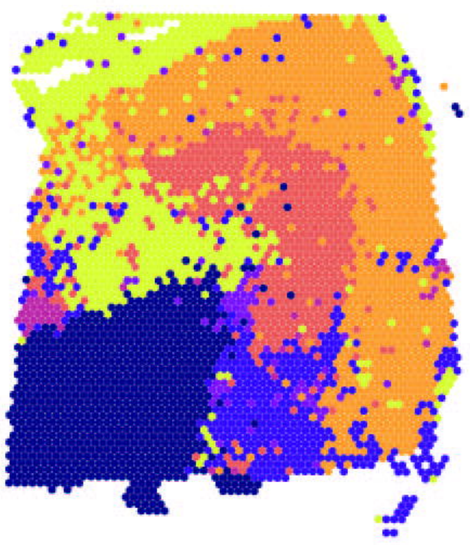

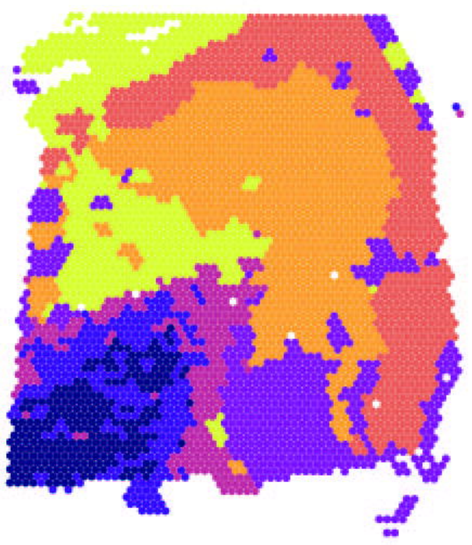

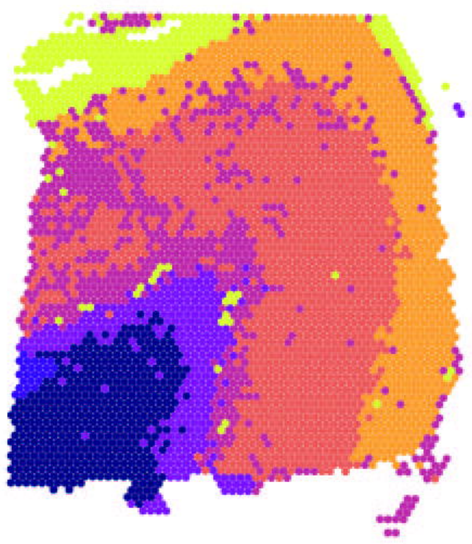

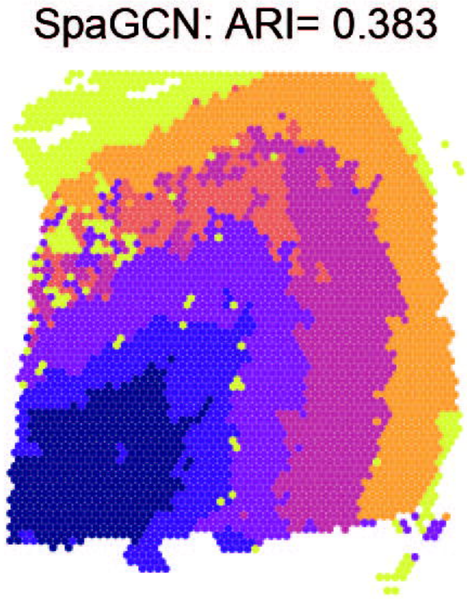

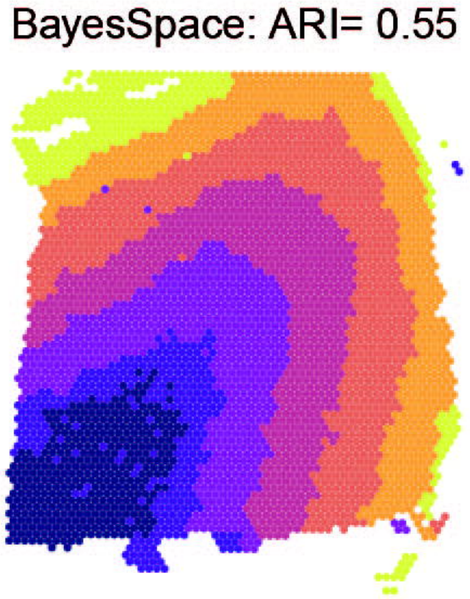

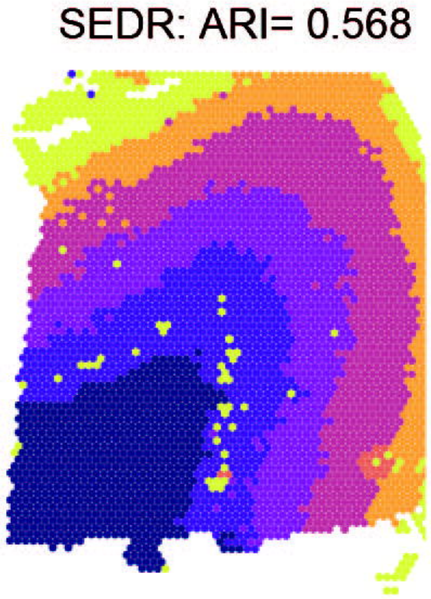

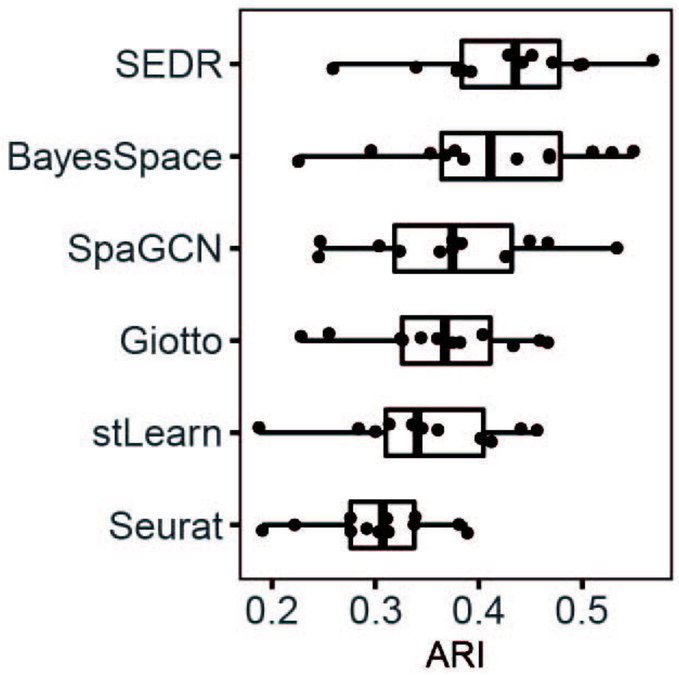

B

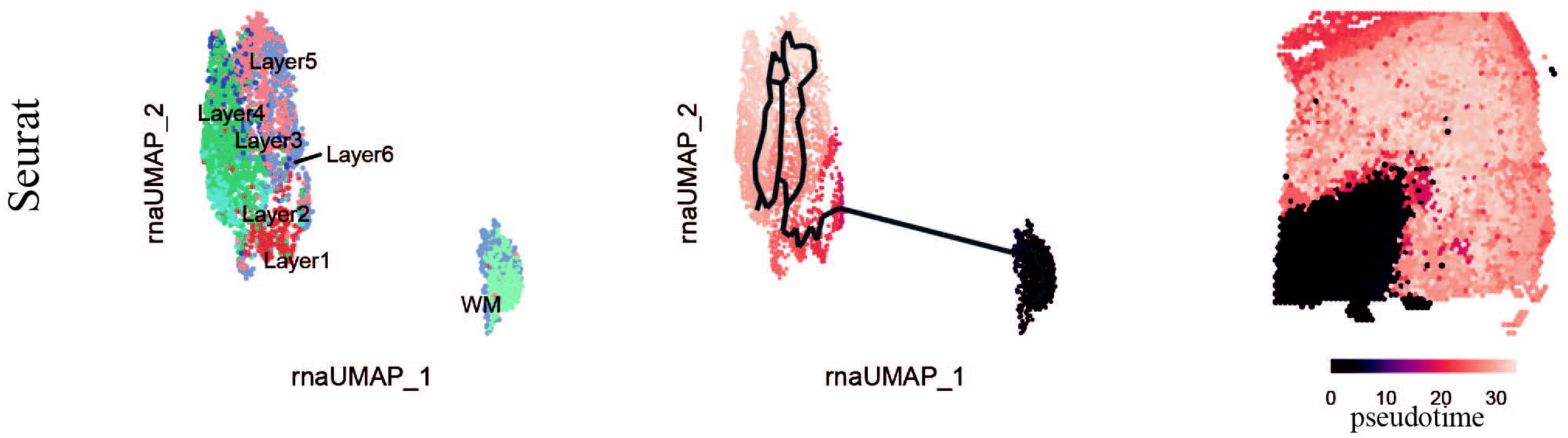

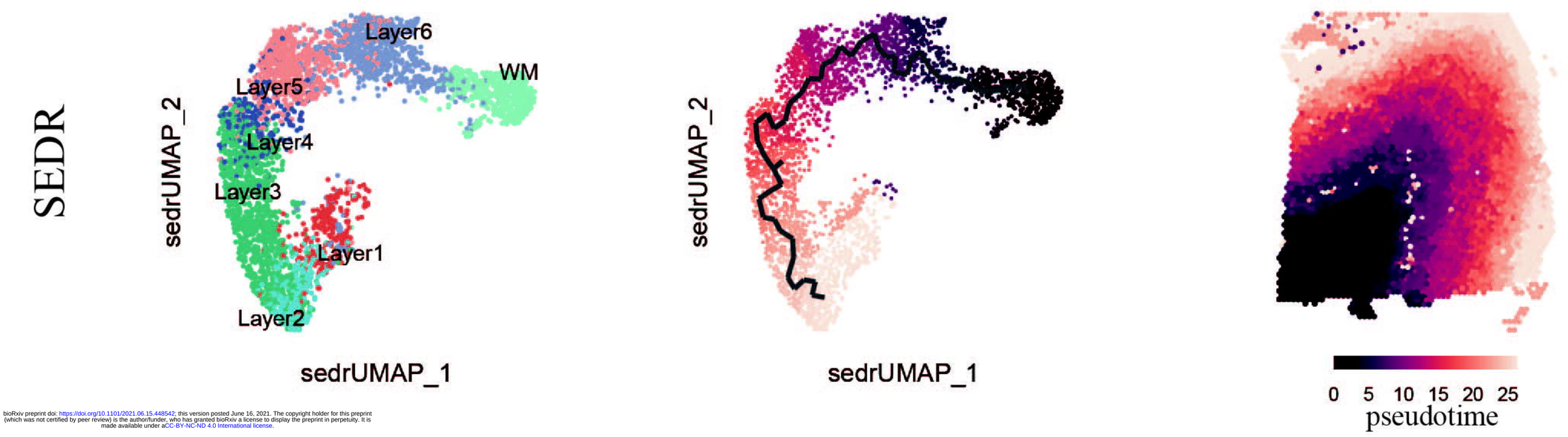

C

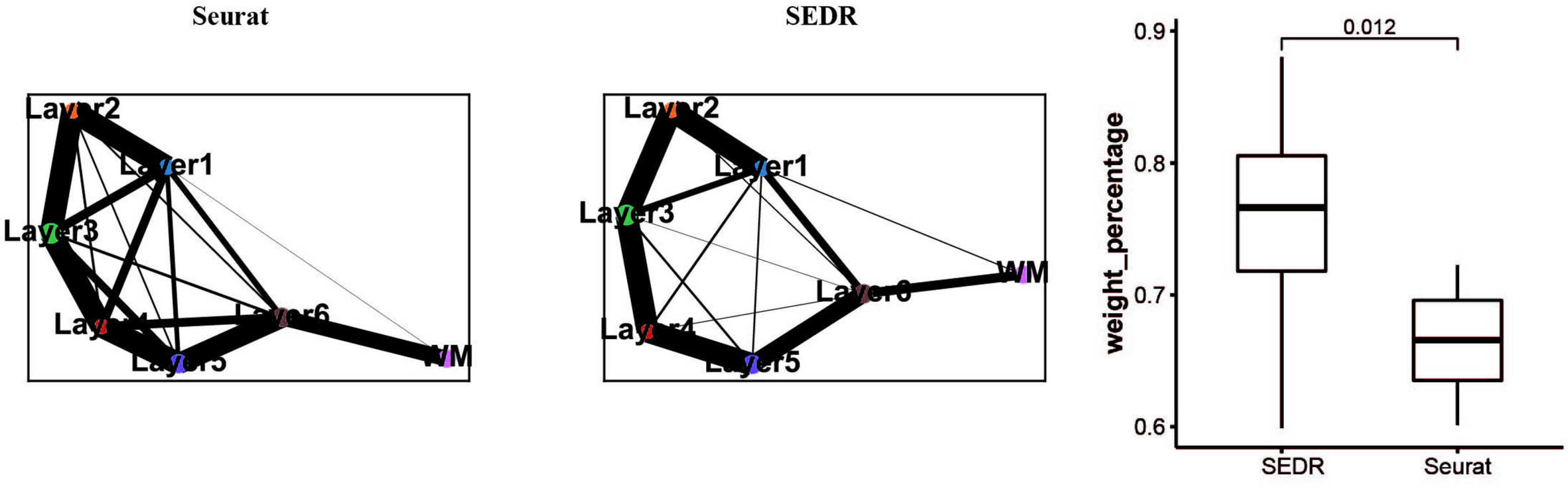

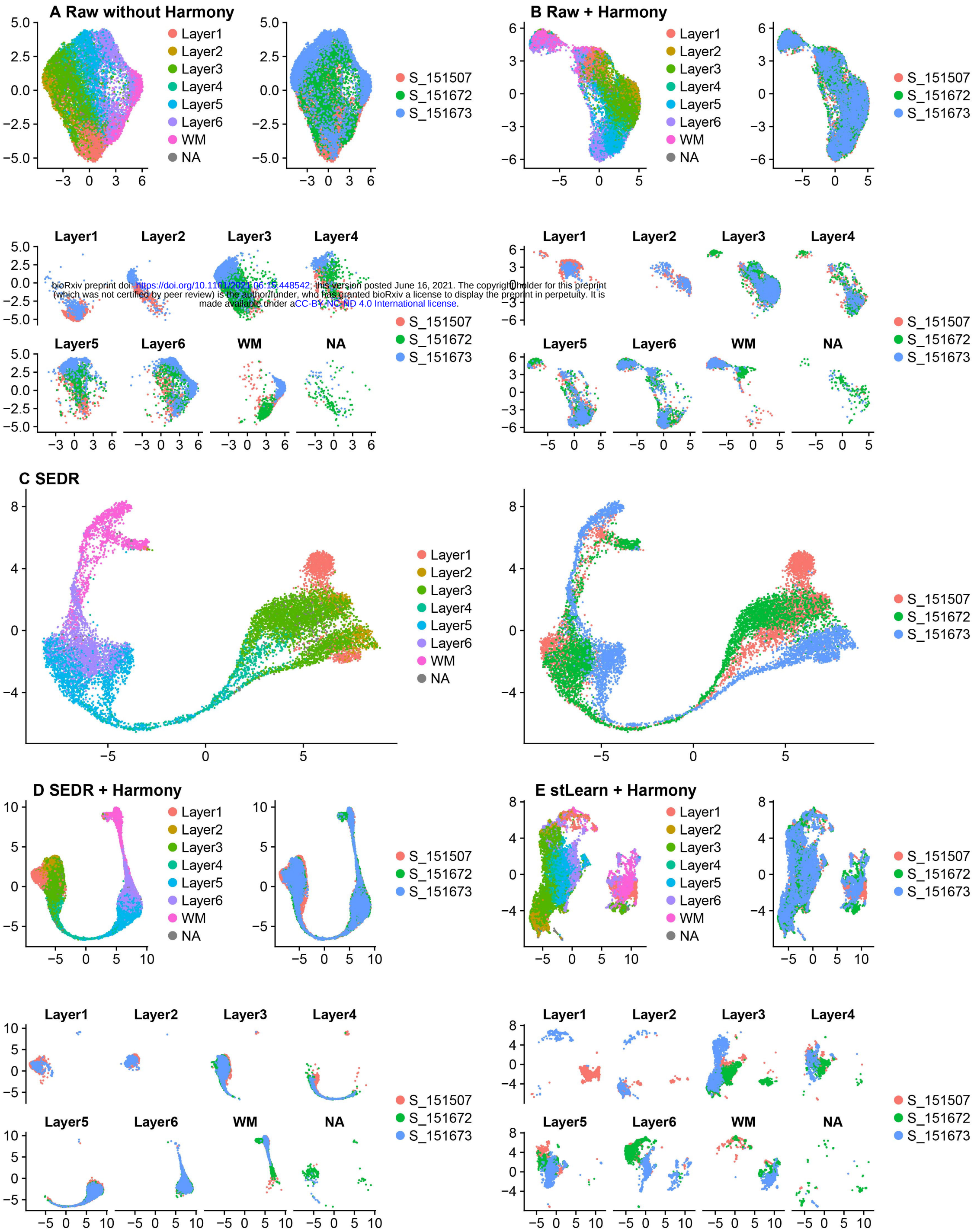

A

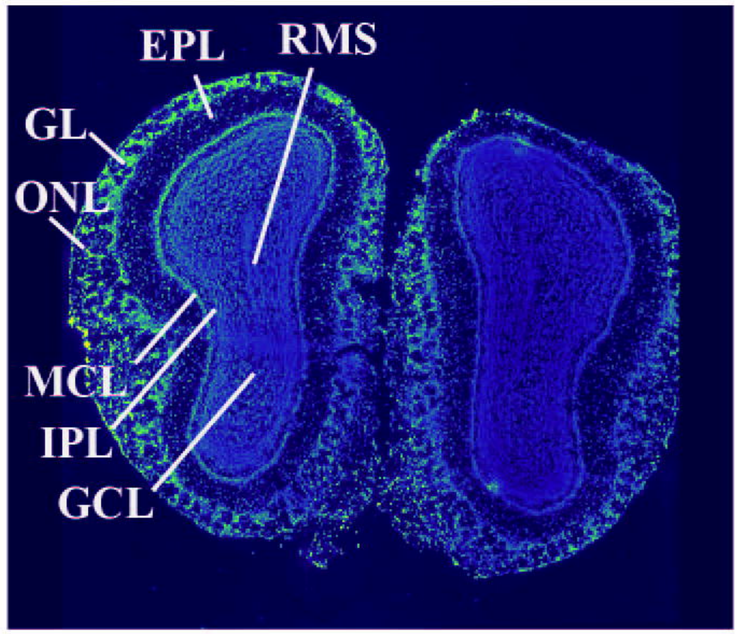

B

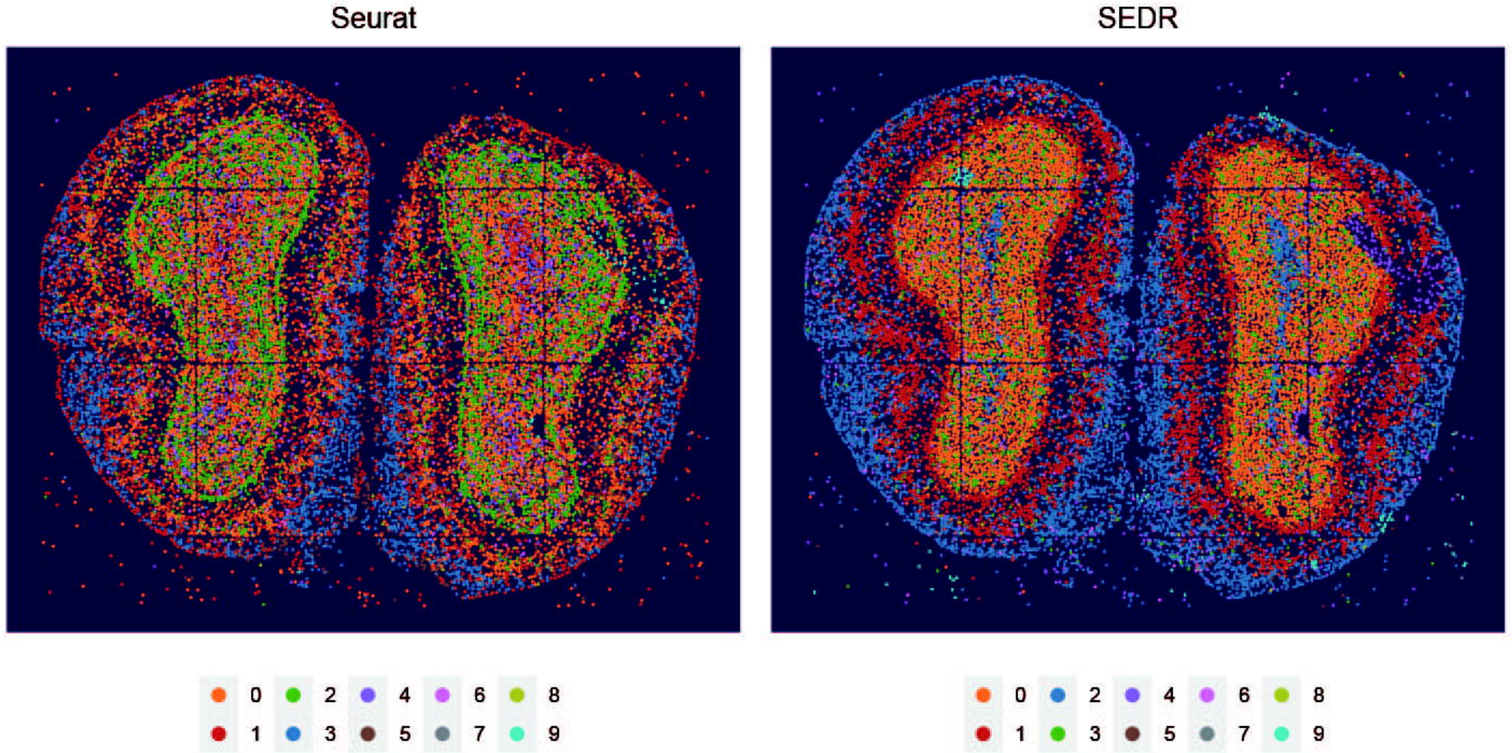

C

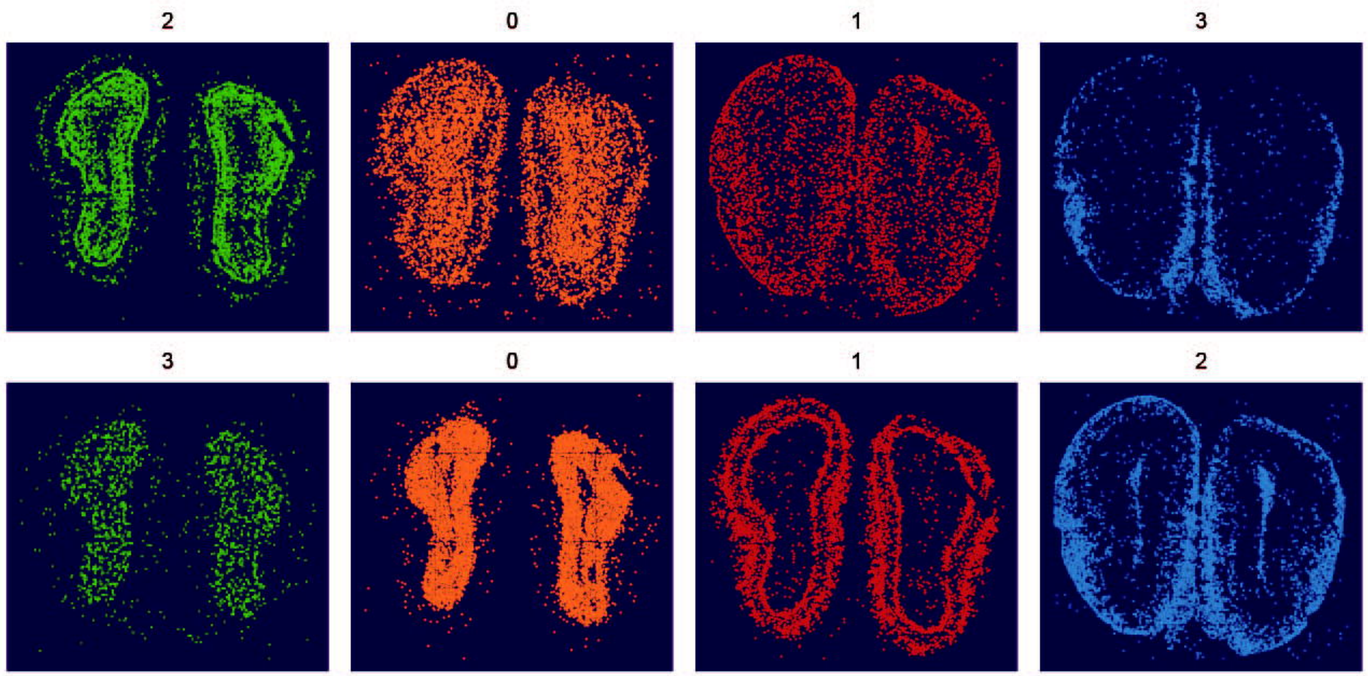

D

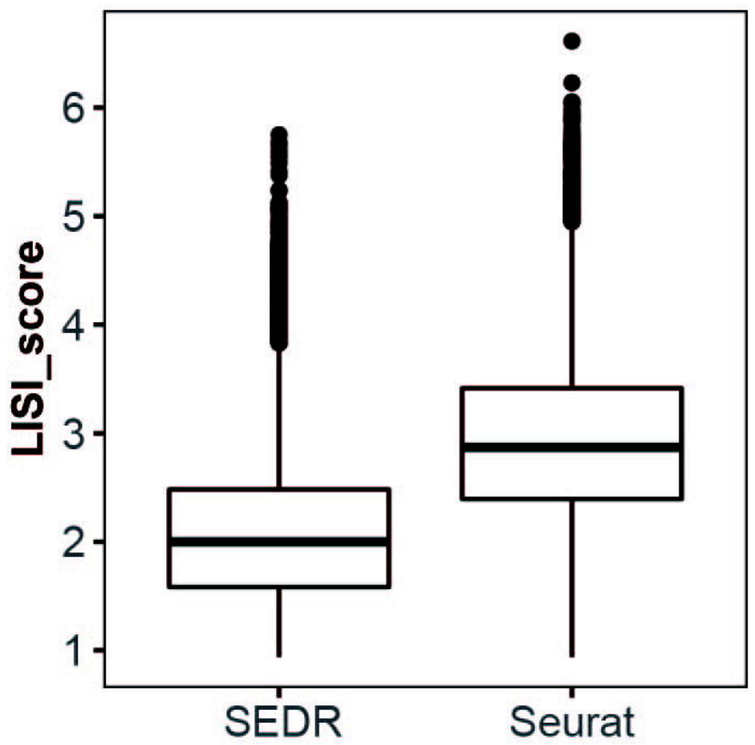

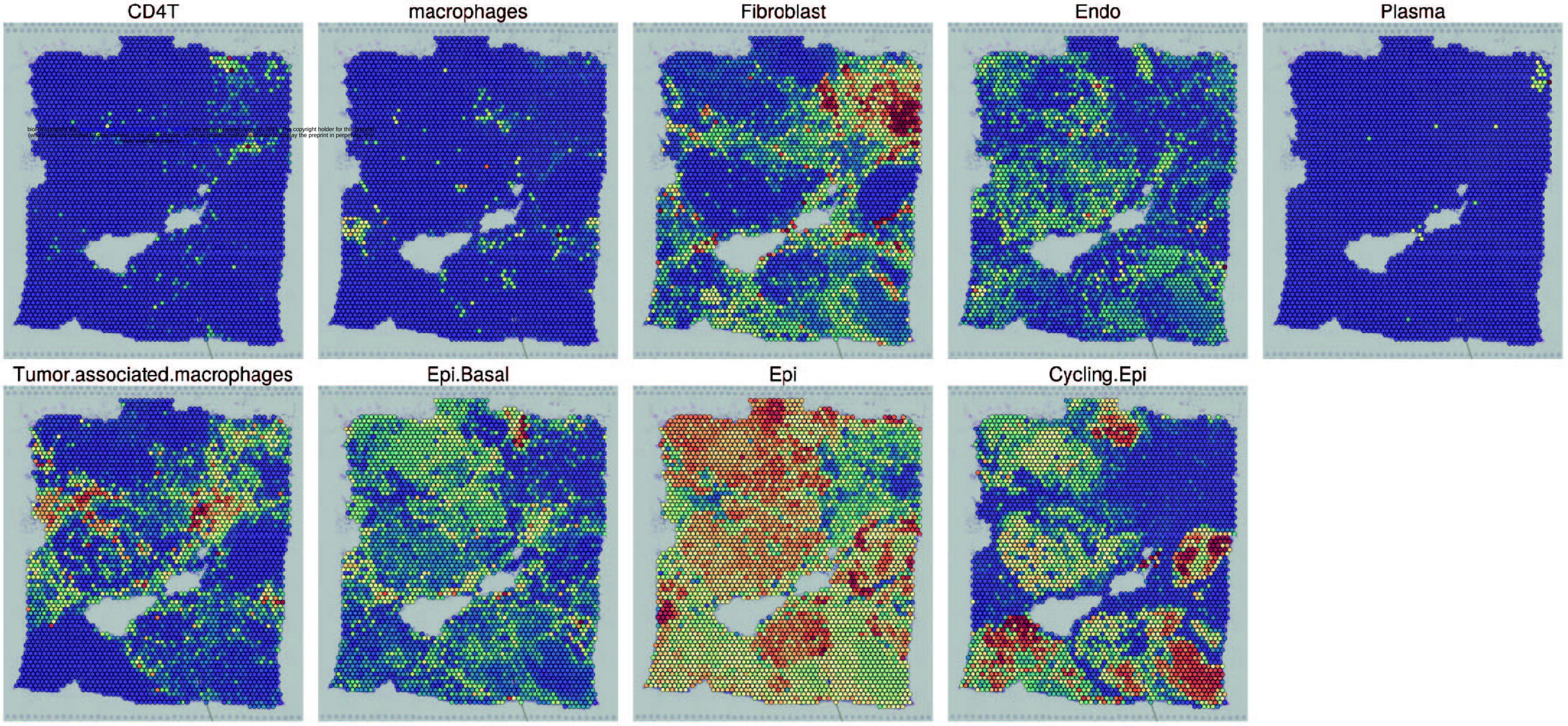

A

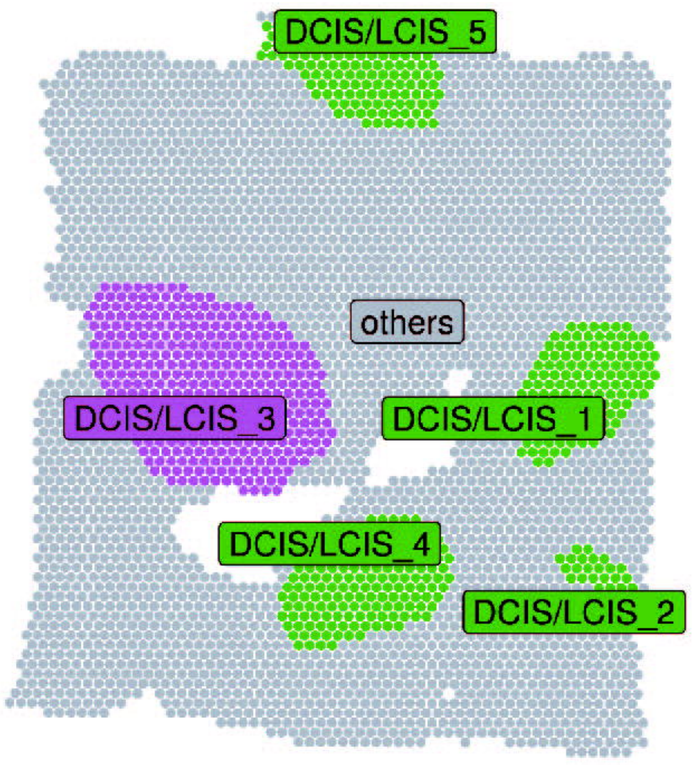

B

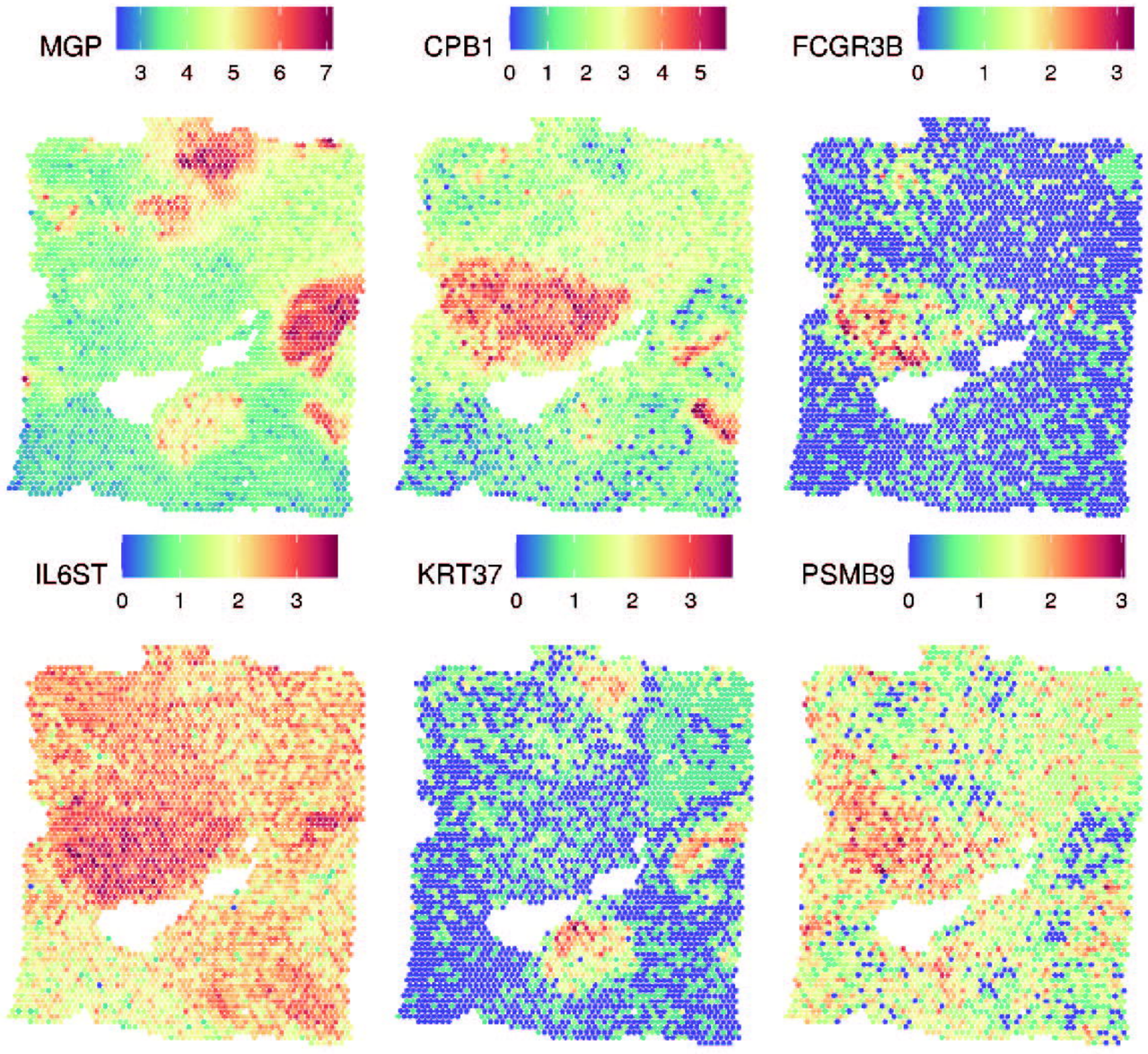

C

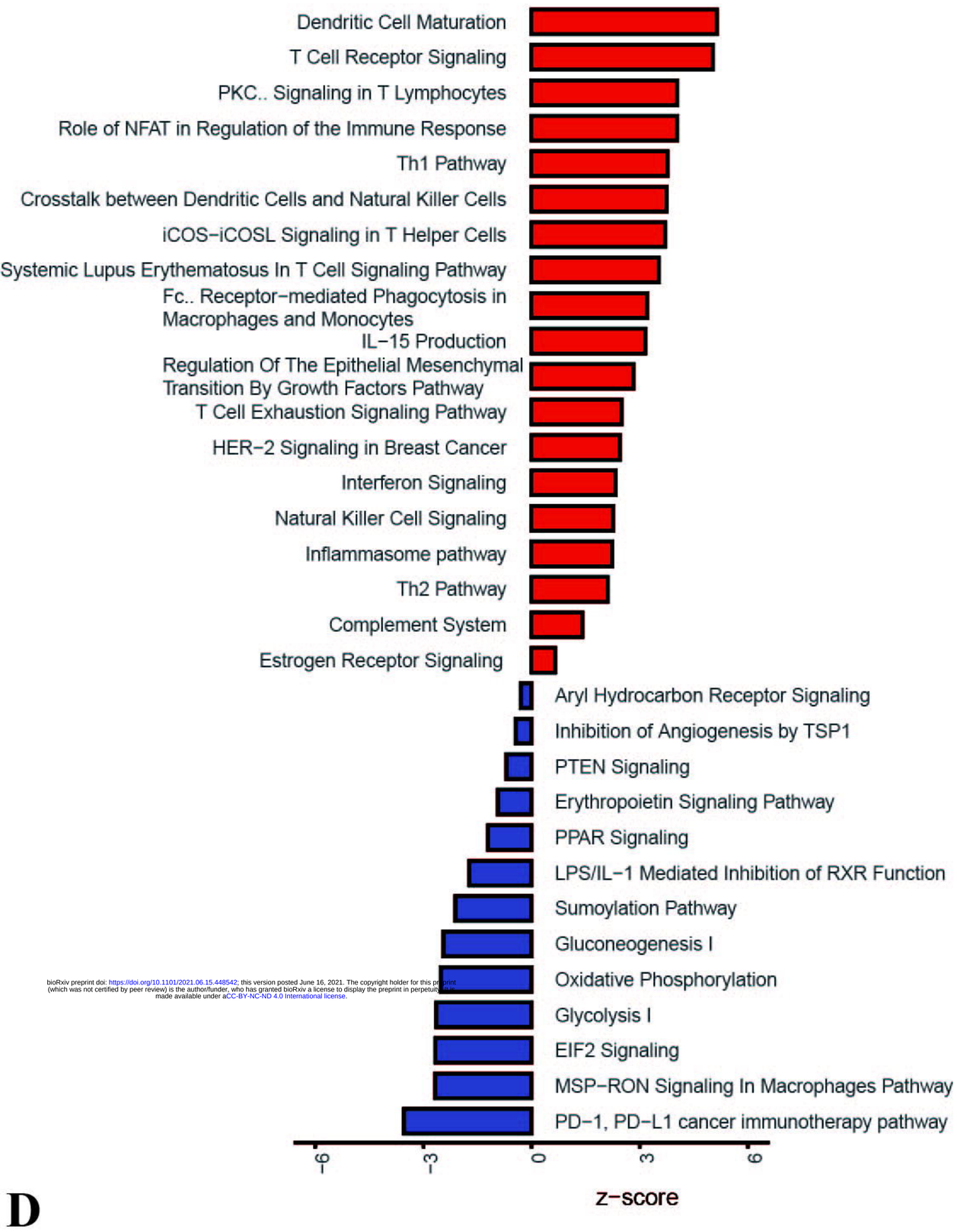

D

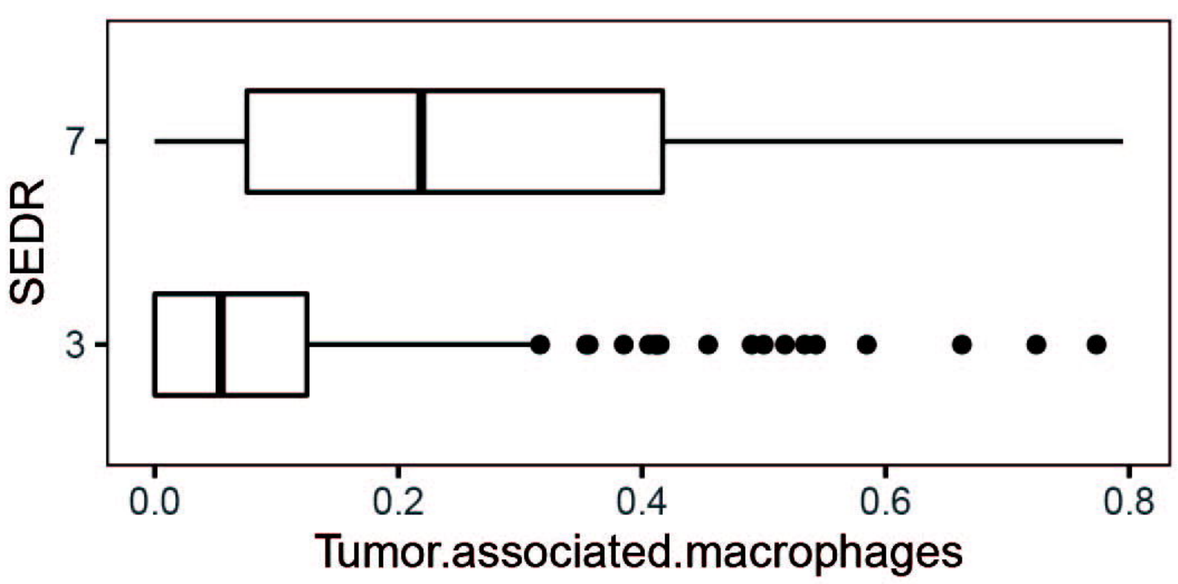

E